Research Article

Humaira Yasmin*, Hala A. Hejazi, Showkat Ahmad Lone, Zehba Raizah, and Anwar Saeed*

Time-independent three-dimensional flow of a water-based hybrid nanofluid past a Riga plate with slips and convective conditions: A homotopic solution

https://doi.org/10.1515/ntrev-2023-0183 received June 27, 2023; accepted December 21, 2023

Abstract: In the present analysis, we have analyzed the three-dimensional flow of an electromagnetohydrodynamic copper-aluminum/water hybrid nanofluid flow on a Riga plate. The heat and mass flux model proposed by Cattaneo-Christov is deliberated here. Thermal radiation, thermophoretic diffusion, Brownian motion, and chemical reaction phenomena are considered in analyzing the flow problem. Thermal convective, mass convective, and velocity slip conditions are adapted in this analysis. Suitable resemblance variables are implemented for the conversion of the model equations to dimension-free form. The homotopy analysis method is adopted to solve the modeled equations. The obtained results show that the velocity profiles are reduced with an increasing estimation of the slip factors. Additionally, the nanoparticles' concentration and the temperature of the hybrid nanofluid increase with higher values of thermal and solutal Biot numbers. The Nusselt number is increased with an increase in the radiation factor and thermal Biot number.

Keywords: nanofluid, hybrid nanofluid, electromagnetohydrodynamic, Riga plate, slip conditions, convective conditions, HAM

* Corresponding author: Humaira Yasmin, Department of Basic Sciences, General Administration of the Preparatory Year, King Faisal University, 31982, Al-Ahsa, Saudi Arabia, e-mail: hhassain@kfu.edu.sa

Hala A. Hejazi: Mathematics Department, Faculty of Sciences, Umm Al-Qura University, Makkah, Saudi Arabia

Showkat Ahmad Lone: Department of Basic Sciences, College of Science and Theoretical Studies, Saudi Electronic University, (Jeddah-M), Riyadh 11673, Kingdom of Saudi Arabia

Zehba Raizah: Department of mathematics, college of Science, King Khalid University, Abha, Saudi Arabia

Nomenclature

constants

a, b

velocity components u, v, w $C_{\rm p}$ specific heat h_{T} convective heat transfer coefficient h_{C} convective mass transfer coefficient thermal relaxation time coefficient mass relaxation time coefficient C_{∞} ambient concentration surface temperature C_{fx} , C_{fy} skin frictions thermal-dependent heat source factor space-dependent heat source factor thermophoresis parameter Nb Brownian motion parameter \boldsymbol{A} modified Hartman number current density magnetization strength $M_0(x)$ $D_{\rm B}$ Brownian diffusivity k^* mean absorption coefficient Е activation energy factor k thermal conductivity Pr Prandtl number

Greek words

dancity

Sc

ρ	uensity
eta_1	thermal Biot number
$oldsymbol{eta}_2$	solutal Biot number
σ^*	Stefan-Boltzmann constant
λ	ratio factor
μ	dynamic viscosity
ξ	similarity variable
γ_1	thermal relaxation parameter

Schmidt number

^{*} Corresponding author: Anwar Saeed, Department of Mathematics, Abdul Wali Khan University, Mardan, 23200, Khyber Pakhtunkhwa, Pakistan, e-mail: anwarsaeed769@gmail.com

 y_2 mass relaxation parameter

 α_1, α_2 slip parameters Sc Schmidt number

 Π volume fraction of the nanoparticle

 σ electrical conductivity

Subscripts

Al₂O₃, Cu nanoparticles hnf hybrid nanofluid

 $\begin{array}{ll}
\text{nf} & \text{nanofluid} \\
\text{f} & \text{base fluid} \\
\infty & \text{free stream}
\end{array}$

1 Introduction

Nanoparticles have significant applications in the industry due to their thermal and rheological characteristics in base fluids, which attracted the attention of many researchers. This type of fluid is known as nanofluid, which can be designed by dangling a monotype of nanoparticles in base fluids. Due to the vast thermal conductivity behavior, these fluids are used for cooling purposes such as electrical devices, nuclear reactors, the coolant of heat exchangers, and the coolant of auto engines, etc. To increase the thermal conductivity of nanofluids, Choi and Eastman [1] have studied the nanoparticles in pure fluids. Ayub et al. [2] observed the upshot of slip-on electro-magnetohydrodynamic nanostructures stream upon a Riga plate. Pal and Mandal [3] considered the behavior of thermodiffusion on a magnetized stagnation point stream over an extending sheet with suction. They found that skin friction reduces with the material factor of the Sisko fluid. Bhatti and Michaelides [4] considered the Arrhenius activation energy feathers on the thermo-bio-convection nanoliquid spreads through a Riga plate. The feathers of variable thermal conductivity and viscosity of a three-dimensional unsteady Maxwell nanofluid on an extending surface were discussed by Ahmed et al. [5]. The results reveal that the Nusselt number shows a decreasing influence because of the unsteadiness factor. Hussain et al. [6] examined the mass and thermal transmission feathers of the MHD rotating nanofluid flow on an extending surface. Makinde and Aziz [7] examined the flow of a boundary layer induced in a nanoliquid on an extending sheet with convective boundary conditions. The decreasing influence is seen in the thermal profile through the Lewis number. Khan et al. [8] explored the two-dimensional aligned MHD motion of nanofluids towards an extending surface with slip condition. From the analysis, it is explored that the flow sketch decays with the slip factor.

A hybrid nanofluid is a kind of fluid that consists of a base fluid such as oil or water, and different types of nanoparticles such as polymers, metals, and ceramics distributed within it. The accumulation of nanostructures into base fluids increased the heat, electrical, and mechanical properties of the fluid. A hybrid nanofluid has many requests in different areas such as in heat exchangers, cooling in an electronic system, medicine distribution, and power plants. Devi and Devi [9] deliberated on the inspiration of suction on the hydromagnetic hybrid nanofluid stream upon a stretching sheet. They concluded that in a magnetic field, the rate of the heat flux of the nanoliquid is more than that of the nanoliquid flow. Yousifi et al. [10] tested the hybrid nanostructure flow of aqueous copper-titanium nanoparticles upon a wavy cylinder. Swain et al. [11] exposed variable magnetic field impressions on a hybrid nanofluid upon a shrinking surface with slip conditions. It is seen that the skin friction falls with a higher slip factor. Joshi et al. [12] inspected the magnetized hybrid nanofluid flow with suction influence in a Darcy-Forchheimer permeable medium. Ramzan et al. [13] investigated the magnetized hybrid nanofluid stream on an extending surface subjected to the influence of velocity and thermal slip conditions. The results reveal that the improvement in the Eckert number increases the Nusselt number. Dawar et al. [14] performed a comparative analysis of the magnetized hybrid nanoliquid upon a spreading surface with slip and convective conditions. The analysis indicated that the flow profile increased with the increasing stretching parameter. Ghadikolaei et al. [15] inspected the magnetized stream and thermal transmission of the micropolar hybrid nanofluid upon a surface with a thermal radiative effect. Gul et al. [16] examined the thermal transmission by an irreversibility study of the couple stress hybrid nanofluid upon a spreading sheet. Md Basir et al. [17] considered the flow of a hybrid nanofluid with the melting thermal transmission and thermal radioactivity effect. They concluded that the thermal transfer rate increases with a larger thermal radiation factor.

The Riga surface, also identified as the Riga plate, is a significant actuator synthesized of magnets and electrodes that produce Lorentz forces, which rapidly move away from the Riga surface. Due to several applications at the industry level, researchers have conducted different analyses for the flow on a Riga plate. Bhatti and Michaelides [4] studied the effect of the Arrhenius activation power on the bioconversion nanofluid stream on a Riga sheet.

The results reveal that the microorganism's outline is decreased with an advanced bioconvection Schmidt number. Rasool et al. [18] considered the Marangoni-based Casson model nanofluid flow under the impact of the Lorentz force produced by the Riga plate. A significant decrease was observed in the flow profile by including the Casson factor. Naseem et al. [19] used the Cattaneo-Christov model to study the third-grade nanofluidic flow upon a Riga plate. The investigation revealed that the higher thermal relaxation factor decreases the temperature profile. Khashi'ie et al. [20] examined the impression of combined convection and suction factors at the stagnant point flow of a hybrid nanoliquid toward a Riga sheet. Alotaibi and Rafique [21] discussed the mass and thermal transferring phenomena of a micropolar nanofluid upon a Riga plate. It has been noticed that the modified Hartman number increases the energy and mass flux rates. The feathers of nonlinear thermal radiation of the electromagnetohydrodynamic (EMHD) fluid flow stream between two Riga surfaces are investigated by Ahmad et al. [22].

In the transportation of heat, thermal radiation plays a key role. The influence of these radiations is attractively dominant in higher thermal practice. A relative study of thermal transmission of the magnetohydrodynamic Jeffery fluid on thermal radiation is studied by Rahman et al. [23]. Eid and Nafe [24] analyzed the influence of the generation of heat and variable thermal conductance on the MHD fluid flow on a permeable medium. The results indicate that the temperature is increased with a large heat generation parameter. Ashraf et al. [25] observed the Darcy-Forchheimer stream of the nanofluid upon an extending revolving inclined disk with the inspiration of thermal radiation. It is noted that with an advanced volume fraction parameter, the fluid temperature is increased. Mandal [26] investigated the radiated convective thermal transmission of the micropolar nanofluid upon an elongating surface. Saeed et al. [27] examined the magnetohydrodynamic Casson hybrid nanofluid stream upon a spreading sheet on a permeable medium with thermally radiative effects. The results show that the concentration panels reduce with the impact of the chemical factor. Dawar et al. [28] studied the two-dimensional electrical conduction nanofluid upon a spreading surface with a strong magnetic field and thermal radiation using a porous medium. It is noted that with nonlinear thermal radiation, the thermal sketch is more highly affected than those of linear thermal radiation.

Brownian diffusion, which is also known as molecular diffusion, is the irregular flow of atoms in a fluid by collisions with other particles. This type of phenomenon occurs in all types of fluids such as gases, liquids, and some solids. Brownian diffusion is the movement of atoms in a fluid due to a temperature gradient. The fluids that have temperature differences will experience a thermophoretic force, which tends to move them from a higher area of temperature to a lower area of temperature. Shah et al. [29] observed the impression of Brownian diffusion and thermophoresis on the suspension of nanoparticles in the convective Maxwell nanofluid. The results show that the thermal conductivity of nanoparticles increases with Brownian motion, which significantly increases the motion of nanoparticles. Kalpana et al. [30] observed the feathers of the MHD fluid flow in a rough channel with the effect of Brownian motion and thermophoresis. This reveals that the increasing magnetic field increased the thermal transfer rate. Igbal et al. [31] studied the behavior of Brownian and thermophoretic diffusions in the MHD Burger nanofluid with convective boundary conditions on an extending cylinder.

From the above study, we observed that no work based on 3D EMHD hybrid nanofluid over a Riga plate with the impacts of thermal-dependent heat source, space-dependent heat source, velocity slips, and thermal and mass convective conditions has been conducted. Therefore, the authors have proposed this analysis to investigate the water-based hybrid nanofluid containing copper and alumina nanoparticles past a Riga plate. Additionally, the Cattaneo-Christov heat and mass flux model along with thermophoresis and Brownian motion has been implemented in the present analysis. To convert the set of the governed flow equation into dimensionless form, suitable similarity variables are used. The homotopy analysis method (HAM) has been implemented for the current flow solution of the hybrid nanofluid flow model. The article is composed of several sections. Section 1 contains the introduction. Section 2 encompasses the problem formulation, where the PDEs are transformed into ODEs using similarity variables. Section 3 includes the HAM solution. Section 4 includes the HAM convergence. Section 5 includes the result and discussion. Section 6 includes the concluding points. The original research questions that are predictable to report in the supposed study are the following: (I) What are the influences of modified Hartman number, stretching ratio, and slip factor hybrid nanofluid flow velocities and skin friction? (II) What are the consequences of thermal relaxation and thermal radiation factors on the hybrid nanofluid flow temperature and heat transfer rate? (III) What are the consequences of the mass relaxation time factor, chemical reaction, and activation energy on the mass concentration profile? (IV) In which case (nanofluid or hybrid nanofluid) do the velocities and thermal profiles show maximum behavior?

2 Problem formulation

Consider the three-dimensional EMHD hybrid nanofluid flow over a bi-directional Riga plate. The sheet stretches along x- and y-directions with velocities $u_w(x) = ax$ and $v_w(x) = by$ where a and b are constants. The surface and the infinite temperatures of the fluid are denoted by T_w and T_∞ , and the fluid concentrations are denoted by C_w and C_∞ . The geometrical representation of the considered flow problem is described in Figure 1. Moreover, the following assumptions are considered:

- Riga plate
- · The exponential and thermal-based heat sources
- Slip and convective conditions
- · Cattaneo-Christov heat and mass flux phenomena
- · Arrhenius activation and thermal radiation effects
- · Thermophoresis diffusion and Brownian motion.

Given the aforementioned assumptions, the primary governing equations can be written as follows: [32–34].

2.1 Continuity equation

$$\frac{\partial v}{\partial v} + \frac{\partial u}{\partial x} + \frac{\partial w}{\partial z} = 0,$$
 (1)

2.2 Momentum equations

$$u\frac{\partial u}{\partial x} + \frac{\partial u}{\partial z}w + v\frac{\partial u}{\partial y} = \frac{\mu_{\rm hnf}}{\rho_{\rm hnf}}\frac{\partial^2 u}{\partial x^2} + \frac{\pi j_0 M_0}{8\rho_{\rm hnf}}e^{\left[-\frac{\pi}{a_0}z\right]}, \quad (2)$$

$$u\frac{\partial v}{\partial x} + v\frac{\partial v}{\partial y} + w\frac{\partial v}{\partial z} = \frac{\mu_{\text{hnf}}}{\rho_{\text{hnf}}} \frac{\partial^2 v}{\partial z^2}.$$
 (3)

2.3 Temperature equation

$$u\frac{\partial T}{\partial x}w\frac{\partial T}{\partial z} + v\frac{\partial T}{\partial y} + \lambda_{E}\sigma_{E}$$

$$= \frac{k_{hnf}}{(\rho C_{p})_{hnf}}\frac{\partial^{2}T}{\partial z^{2}} + \frac{(\rho \tilde{C}_{p})_{np}}{(\rho \tilde{C}_{p})_{hnf}}\left[D_{B}\frac{\partial C}{\partial z}\frac{\partial T}{\partial z} + \frac{D_{T}}{T_{\infty}}\left(\frac{\partial T}{\partial z}\right)^{2}\right]$$

$$+ \frac{1}{(\rho \tilde{C}_{p})_{hnf}}\left[Q_{0}(T - T_{\infty}) + Q_{1}(T_{f} - T_{\infty})e^{-n\xi} - \frac{\partial q_{z}}{\partial z}\right],$$

$$u = u_{w}(x) + u_{d}\left(\frac{\partial T}{\partial z}\right), v = 0,$$

$$-k_{hnf}\frac{\partial T}{\partial z} = h_{T}(T_{f} - T),$$

$$-D_{B}\frac{\partial C}{\partial z} = h_{C}(C_{f} - C),$$

$$u = 0, v \neq 0, C \neq C,$$

$$u \neq 0, v \neq 0, C \neq C,$$

2.4 Concentration equation

$$u\frac{\partial C}{\partial x} + v\frac{\partial C}{\partial y} + w\frac{\partial C}{\partial z} + \lambda_C \sigma_C$$

$$= \frac{D_T}{T_\infty} \left(\frac{\partial^2 T}{\partial z^2} \right) + D_B \frac{\partial^2 C}{\partial z^2} - K_r^2 (C - C_\infty) \left(\frac{T}{T_\infty} \right)^m e^{-\frac{E_a}{\kappa T}}.$$
(5)

In Eqs. (4) and (5), the Cattaneo–Christov heat flux (σ_E) and mass flux (σ_C) equations are defined as

$$\sigma_{\rm E} = \begin{cases} u^2 \frac{\partial^2 T}{\partial x^2} + w^2 \frac{\partial^2 T}{\partial z^2} + v^2 \frac{\partial^2 T}{\partial y^2} + 2uv \frac{\partial^2 T}{\partial x \partial y} \\ + 2wu \frac{\partial^2 T}{\partial x \partial z} + 2wv \frac{\partial^2 T}{\partial y \partial z} \\ + \left[u \frac{\partial u}{\partial x} + v \frac{\partial u}{\partial y} + w \frac{\partial u}{\partial z} \right] \frac{\partial T}{\partial x} + \left[v \frac{\partial v}{\partial y} + u \frac{\partial v}{\partial x} \right] \\ + w \frac{\partial v}{\partial z} \frac{\partial T}{\partial y} + \left[v \frac{\partial w}{\partial y} + u \frac{\partial w}{\partial x} + w \frac{\partial w}{\partial z} \right] \frac{\partial T}{\partial z} \end{cases}$$
(6)

$$\sigma_{C} = \begin{cases} u^{2} \frac{\partial^{2} C}{\partial x^{2}} + w^{2} \frac{\partial^{2} C}{\partial z^{2}} + v^{2} \frac{\partial^{2} C}{\partial y^{2}} + 2uv \frac{\partial^{2} C}{\partial x \partial y} \\ + 2wu \frac{\partial^{2} C}{\partial x \partial z} + 2wv \frac{\partial^{2} C}{\partial y \partial z} \\ + \left[u \frac{\partial u}{\partial x} + v \frac{\partial u}{\partial y} + w \frac{\partial u}{\partial z} \right] \frac{\partial C}{\partial x} + \left[v \frac{\partial v}{\partial y} + u \frac{\partial v}{\partial x} \right] \frac{\partial C}{\partial z} \\ + w \frac{\partial v}{\partial z} \frac{\partial C}{\partial y} + \left[v \frac{\partial w}{\partial y} + u \frac{\partial w}{\partial x} + w \frac{\partial w}{\partial z} \right] \frac{\partial C}{\partial z} \end{cases}$$
(7)

The radiative heat flux (q_r) is defined as

$$q_{\rm r} = -\frac{4\sigma^*}{3k^*} \frac{\partial T^4}{\partial \sigma}, \quad T^4 \cong 4T_{\infty}^3 T - 3T_{\infty}^4.$$
 (8)

Eq. (6) represents the Cattaneo-Christov heat flux model, Eq. (7) represents the Cattaneo-Christov mass flux model, and Eq. (8) represents the thermal radiation heat flux phenomenon.

2.5 Boundary conditions

The boundary conditions are defined as

$$u = u_{w}(x) + \alpha_{a} \left(\frac{\partial u}{\partial z} \right), \quad v = v_{w}(y) + \alpha_{b} \left(\frac{\partial v}{\partial z} \right),$$

$$w = 0,$$

$$-k_{hnf} \frac{\partial T}{\partial z} = h_{T}(T_{f} - T),$$

$$-D_{B} \frac{\partial C}{\partial z} = h_{C}(C_{f} - C),$$

$$u \to 0, \quad v \to 0, \quad C \to C_{\infty}, \quad T \to T_{\infty} \} \text{ as } z \to \infty.$$

$$(9)$$

Table 1 demonstrates the thermophysical relations of the hybrid nanofluid and nanofluid, and Table 2 lists the experimental values of the thermophysical properties.

Here, Π_1 and Π_2 represent the volume fractions of Cu and Al₂O₃ nanoparticles, s_1 represents the Cu nanoparticle, and s_2 represents the Al₂O₃ nanoparticle. The density, dynamic viscosity, specific heat, electrical conductivity,

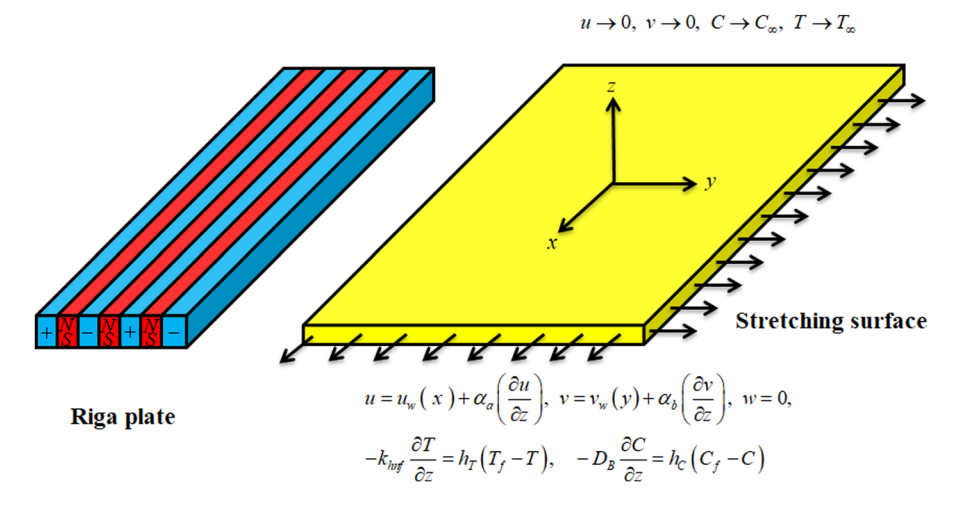


Figure 1: Geometry of flow problem.

and thermal conductivity are denoted by ρ , μ , $\tilde{C}_{\rm p}$, σ , and k, respectively. The subscripts f, nf, and hnf represent the fluid, nanofluid, and hybrid nanofluid, respectively.

The similarity variables are defined as

$$u = axf'(\xi), \ v = ayg'(\xi), \ w = -\sqrt{av_{\rm f}}(f(\xi) + g(\xi)),$$
$$\xi = \sqrt{\frac{a}{v_{\rm f}}}z, \ \phi(\xi) = \frac{C - C_{\infty}}{C_{\rm f} - C_{\infty}}, \ \theta(\xi) = \frac{T - T_{\infty}}{T_{\rm f} - T_{\infty}}. \tag{10}$$

Using these transformations, the leading equations are reduced to

$$\frac{\mu_{\rm hnf}}{\mu_{\rm f}}f''' + \frac{\rho_{\rm hnf}}{\rho_{\rm f}}((f+g)f'' - f'^2) + Ae^{-\beta\xi} = 0, \eqno(11)$$

$$\frac{\mu_{\rm hnf}}{\mu_{\rm f}}g''' + \frac{\rho_{\rm hnf}}{\rho_{\rm f}}((f+g)g' - g'^2) = 0, \tag{12}$$

Table 1: Thermophysical relations of the nanofluid and hybrid nanofluid [35,36]

Properties	Nanofluid
Viscosity	$\mu_{\rm nf} = \frac{\mu_{\rm f}}{(1-H)^{2.5}}$
Density	$\rho_{\rm nf} = (1 - \Pi)\rho_{\rm f} + \Pi\rho_{\rm s}$
Heat capacity	$(ho \tilde{C}_{ m p})_{ m nf} = (ho \tilde{C}_{ m p})_{ m f} (1 - \Pi) + \Pi (ho \tilde{C}_{ m p})_{ m s},$
	$\rho_{\rm hnf} = (1 - \Pi)\rho_{\rm f} + \Pi\rho_{\rm s}$
Electrical	$\frac{\sigma_{\rm nf}}{\sigma_{\rm f}} = 1 + \frac{3II(\sigma - 1)}{(\sigma + 2) + II(\sigma - 1)II}$, where $\sigma = \frac{\sigma_{\rm S}}{\sigma_{\rm f}}$
conductivity	$O_{\mathbf{f}} = (O + 2) + H(O - 1)H$
Thermal	$\frac{k_{\text{nf}}}{k_{\text{f}}} = \frac{k_{\text{s}} + (n-1)k_{\text{f}} - II(k_{\text{f}} - k_{\text{s}})(n-1)}{k_{\text{s}} + k_{\text{f}}(n-1) + (k_{\text{f}} - k_{\text{s}})II}$
conductivity	$\kappa_{\mathbf{f}} \qquad \kappa_{\mathbf{S}} + \kappa_{\mathbf{f}}(n-1) + (\kappa_{\mathbf{f}} - \kappa_{\mathbf{S}})H$

Properties	Hybrid nanofluid
Dynamic viscosity	$\mu_{\rm hnf} = \frac{\mu_{\rm f}}{(1 - H_2 - H_1)^{2.5}}$
Heat capacity	$(\rho \tilde{\mathcal{C}}_{\rm p})_{\rm hnf} = \{[(1 - \Pi_1)(\rho \tilde{\mathcal{C}}_{\rm p})_{\rm f} + \Pi_1(\rho \tilde{\mathcal{C}}_{\rm p})_{s_1}](1 - \Pi_2)\} + \Pi_2(\rho \tilde{\mathcal{C}}_{\rm p})_{s_2}$
Density	$\rho_{\rm hnf} = \{ [(1 - \Pi_1)\rho_{\rm f} + \Pi_1\rho_{\rm s_1}](1 - \Pi_2) \} + \Pi_2\rho_{\rm s_2}$
Electrical conductivity	$\frac{\sigma_{\rm hnf}}{\sigma_{\rm bf}} = \frac{\sigma_{\rm s_2} + 2\sigma_{\rm bf} - 2(\sigma_{\rm bf} - \sigma_{\rm s_2})II_2}{2\sigma_{\rm bf} + \sigma_{\rm s_2} + (\sigma_{\rm bf} - \sigma_{\rm s_2})II_2}, \text{ where } \frac{\sigma_{\rm bf}}{\sigma_{\rm f}} = \frac{2\sigma_{\rm f} + \sigma_{\rm s_1} - 2II_1(\sigma_{\rm f} - \sigma_{\rm s_1})}{2\sigma_{\rm f} + \sigma_{\rm s_1} + II_1(\sigma_{\rm f} - \sigma_{\rm s_1})}$
Thermal conductivity	$\frac{k_{\rm hnf}}{k_{\rm bf}} = \frac{k_{\rm S2} + k_{\rm bf}(n-1) - (n-1)\Pi_2(k_{\rm bf} - k_{\rm S2})}{k_{\rm S2} + k_{\rm bf}(n-1) + \Pi_2(k_{\rm bf} - k_{\rm S2})}$
	where $\frac{k_{\mathrm{bf}}}{k_{\mathrm{f}}} = \frac{k_{\mathrm{s1}} + k_{\mathrm{f}}(n-1) - (n-1)(k_{\mathrm{f}} - k_{\mathrm{s1}})\Pi_{\mathrm{1}}}{k_{\mathrm{s1}} + k_{\mathrm{f}}(n-1) + (k_{\mathrm{f}} - k_{\mathrm{s1}})\Pi_{\mathrm{1}}}$

6 — Humaira Yasmin et al. DE GRUYTER

Table 2: Thermophysical characteristics of the nanoparticles and pure fluid [37–39]

Physical properties	H ₂ O	Al_2O_3	Cu
$\rho[\text{kg/m}^3]$	997.1	3,970	8,933
$\tilde{C}_{\mathrm{p}}[\mathrm{JK/gK}]$	41,790	765	385
σ[S/m]	0.05	1×10^{-7}	5.96×10^{-7}
k[W/mK]	0.613	40	401

$$\begin{split} &\frac{(\rho\tilde{C}_{p})_{f}}{(\rho\tilde{C}_{p})_{hnf}} \left[\frac{k_{hnf}}{k_{f}} + \text{Rd} \right] \theta'' + \text{Pr}(f + g)\theta' \\ &- \frac{(\rho\tilde{C}_{p})_{f}}{(\rho\tilde{C}_{p})_{hnf}} \text{Pr}(\text{Nb}\theta'\phi' + \text{Nt}\theta'^{2}) + \text{Pr} \frac{(\rho\tilde{C}_{p})_{f}}{(\tilde{C}_{p})_{hnf}} Q_{T}\theta \\ &- \text{Pr}\gamma_{1}((f' + g')\theta'(f + g)) - \text{Pr}\gamma_{1}((f^{2} + g^{2} + 2fg)\theta'') \\ &+ \text{Pr} \frac{(\rho\tilde{C}_{p})_{f}}{(\rho\tilde{C}_{p})_{hnf}} Q_{E}e^{-n\xi} = 0, \end{split}$$

$$(13)$$

$$\phi'' + \text{Sc}(f+g)\phi' + \frac{\text{Nt}}{\text{Nb}}\theta'' - \gamma_2 \text{Sc}((f+g)(f'+g'))\phi' - \gamma_2 \text{Sc}(g^2 + f^2 + 2fg)\phi'' - \text{Sc}K_r(1 + \delta\theta)^m e^{-\frac{E}{1+\delta\theta}}\phi$$
= 0. (14)

The boundary conditions are

$$f(0) = 0, \ g(0) = 0, \ f'(0) = 1 + \alpha_1 f''(0),$$

$$g'(0) = \lambda + \alpha_2 g''(0),$$

$$\frac{k_{\text{hnf}}}{k_f} \theta'(0) = \beta_1(\theta(0) - 1), \quad \phi'(0) = \beta_2(\phi(0) - 1),$$

$$f'(\infty) \to 0, \ g'(\infty) \to 0, \ \theta(\infty) \to 0, \ \phi(\infty) \to 0,$$

$$(15)$$

where $A=\frac{\pi M_0 J_0}{8a \rho_f u_w(x)}$ is the modified Hartman number, ${\rm Rd} = \frac{16\sigma^* T_\infty^3}{3k^* k_f} \ \, {\rm is} \ \, {\rm the \ thermal \ radiation \ } \, {\rm factor}, \ \, {\rm Pr} = \frac{(\mu \tilde{C}_p)_f}{k_f} \ \, {\rm is}$

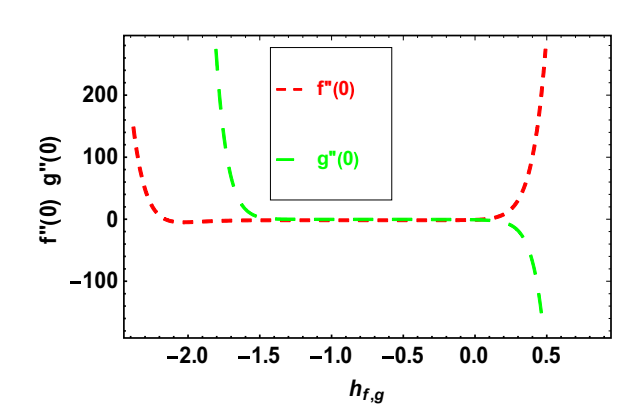


Figure 2: \hbar -curves for velocity profiles $f''(\xi)$ and $g''(\xi)$.

the Prandtl number, Nb = $\frac{(\rho \tilde{c}_p)_{np}}{(\rho \tilde{c}_p)_{f}} \frac{D_B(C_f - C_\infty)}{v_f}$ is the Brownian motion factor, Nt = $\frac{(\rho \tilde{c}_p)_{np}}{(\rho \tilde{c}_p)_f} \frac{D_B(C_f - C_\infty)}{T_\infty v_f}$ is the thermophoresis factor, $Q_T = \frac{Q_0}{a(\rho \tilde{c}_p)_f}$ is the thermal-dependent heat source factor, $Q_E = \frac{Q_1}{a(\rho \tilde{c}_p)_f}$ is the space-dependent heat source factor, $\gamma_1 = \lambda_E a$ is the thermal relaxation parameter, Sc = $\frac{v_f}{D_B}$ is the Schmidt number, $\gamma_2 = \lambda_C a$ is the mass relaxation parameter, $K_r = \frac{K_r^2}{a}$ is the chemical reaction parameter, $\delta = \frac{T_f - T_\infty}{T_\infty}$ is the temperature difference factor, $\epsilon = \frac{E_a}{kT_\infty}$ is the activation energy, $\epsilon = \frac{b}{a}$ is the ratio factor, $\epsilon = \frac{E_a}{kT_\infty}$ and $\epsilon = \frac{a_0\sqrt{v_f}}{a}$ are the velocity slip parameters, and $\epsilon = \frac{h_T}{k_f}\sqrt{v_f}$ and $\epsilon = \frac{h_C}{D_B}\sqrt{v_f}$ are thermal and concentration Biot numbers.

The physical quantities are defined as

$$C_{fx} = \frac{\mu_{hnf} \frac{\partial u}{\partial z} \Big|_{z=0}}{\rho_{f} u_{w}^{2}}, C_{fy} = \frac{\mu_{hnf} \frac{\partial v}{\partial z} \Big|_{z=0}}{\rho_{f} v_{w}^{2}},$$

$$Nu_{x} = \frac{-x k_{hnf} \frac{\partial T}{\partial z} \Big|_{z=0} + q_{z}|_{z=0}}{k_{f} (T_{f} - T_{\infty})}, Sh_{x} = -\frac{x D_{B} \frac{\partial C}{\partial z} \Big|_{z=0}}{D_{B} (C_{f} - C_{\infty})},$$
(16)

where

$$C_{fx} = \frac{\mu_{hnf}}{\mu_f} f''(0), \quad C_{fy} = \frac{\mu_{hnf}}{\mu_f} g''(0),$$

$$\frac{Nu_x}{\sqrt{Re_x}} = -\left(\frac{k_{hnf}}{k_f} + Rd\right) \theta'(0), \quad \frac{Sh_x}{\sqrt{Re_x}} = -\phi'(0).$$
(17)

with $Re_x = \frac{u_w(x)x}{v_f}$ and $Re_y = \frac{v_w(y)y}{v_f}$ being the local Reynolds numbers.

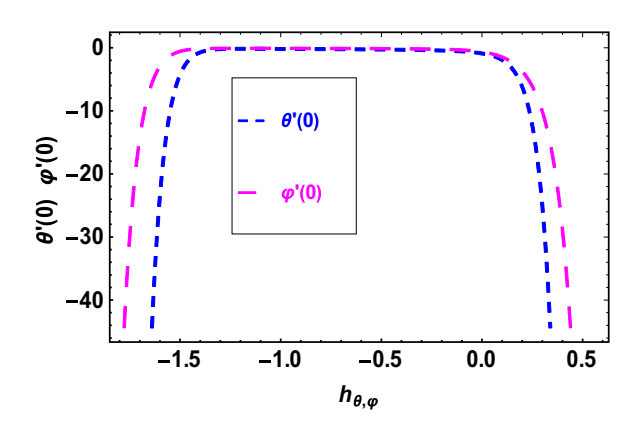


Figure 3: \hbar -curves for temperature and concentration profiles $\theta(\xi)$ and $\phi(\xi)$.

3 HAM solution

HAM is a very effective solution tool for the solution of nonlinear problems, which was first introduced by Liao [40] in 1992. The concept of homotopy is taken from topology to obtain the convergence solution of nonlinear systems. To solve the modeled equations, the initial assumptions are defined as

$$f_0(\xi) = \frac{1}{1 + \alpha_1} (1 - e^{-\xi}), \ g_0(\xi) = \frac{\lambda}{1 + \alpha_2} (1 - e^{-\xi}),$$

$$\theta_0(\xi) = \frac{\beta_1}{(k_{\text{hnf}}/k_{\text{f}}) + \beta_1} e^{-\xi},$$

$$\phi_0(\xi) = \frac{\beta_2}{1 + \beta_2} e^{-\xi}.$$
(18)

The linear operators are delineated as

$$L_f(\xi) = f''' - f, \quad L_g(\xi) = g''' - g,$$

 $L_{\theta}(\xi) = \theta'' - \theta, \quad L_{\phi}(\xi) = \phi'' - \phi.$ (19)

With the following properties:

$$L_{f}(\Delta_{1} + \Delta_{2}e^{-\xi} + \Delta_{3}e^{\xi}) = 0,$$

$$L_{g}(\Delta_{4} + \Delta_{5}e^{-\xi} + \Delta_{6}e^{\xi}) = 0,$$

$$L_{\theta}(\Delta_{7}e^{-\xi} + \Delta_{8}e^{\xi}) = 0,$$

$$L_{\phi}(\Delta_{9}e^{-\xi} + \Delta_{10}e^{\xi}) = 0,$$
(20)

where $\Delta_1 - \Delta_9$ are constants. For further insights into the HAM, one can refer to previous studies [41–43].

4 HAM convergence

In this section, we discuss the convergence of the series solution of the problem through the auxiliary factor \hbar . The \hbar -curves for the velocities, thermal, and concentration

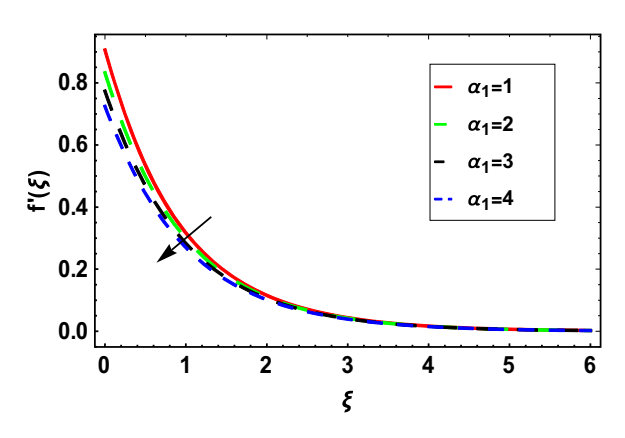


Figure 4: Variation in the velocity profile $f'(\xi)$ *via* the slip parameter α_1 .

profiles are shown in Figures 2 and 3. The area of convergence of \hbar_f , \hbar_g , \hbar_θ , and \hbar_ϕ are $-2.15 \le \hbar_f 0.25$, $-1.5 \le \hbar_g 0.25$, $-1.45 \le \hbar_\theta 0.25$, and $-1.75 \le \hbar_\theta 0.28$, respectively.

5 Results and discussion

The section presents the physical discussion of some embedded factors on the flow velocities, temperature and concentration profiles, skin friction, and Sherwood and Nusselt numbers. The results are shown in Figures 4–19 and Tables 4–8.

5.1 Velocity profiles

The increasing value of slip factors is affected by decreasing both the velocity profiles $f'(\xi)$ and $g'(\xi)$ of the hybrid nanofluid, as shown in Figures 4 and 5. Physically, with the larger

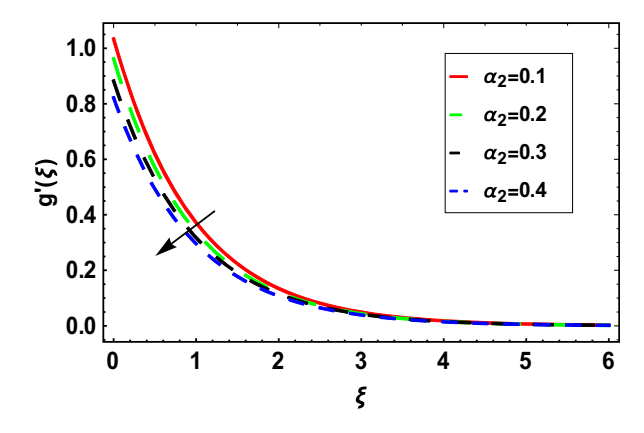


Figure 5: Variation in the velocity profile $g'(\xi)$ via the slip parameter α_2 .

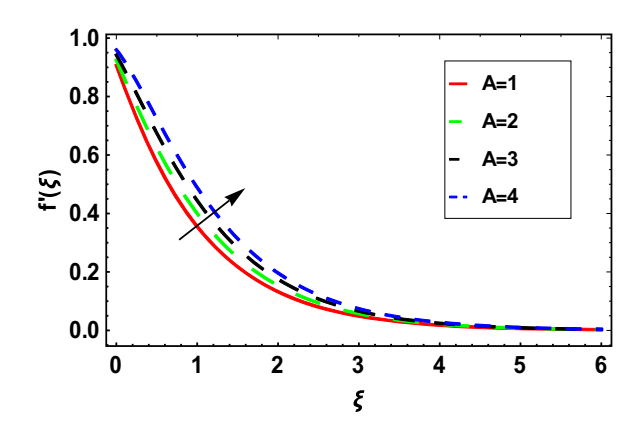


Figure 6: Variation in the velocity profile $f'(\xi)$ *via* the Hartman number A.

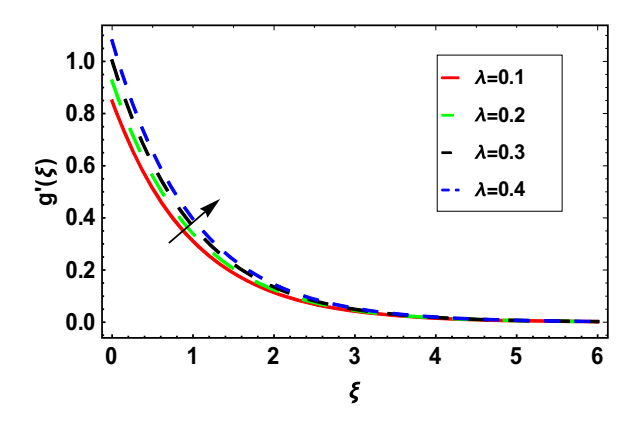


Figure 7: Variation in the velocity profile $g'(\xi)$ via the stretching ratio parameter λ .

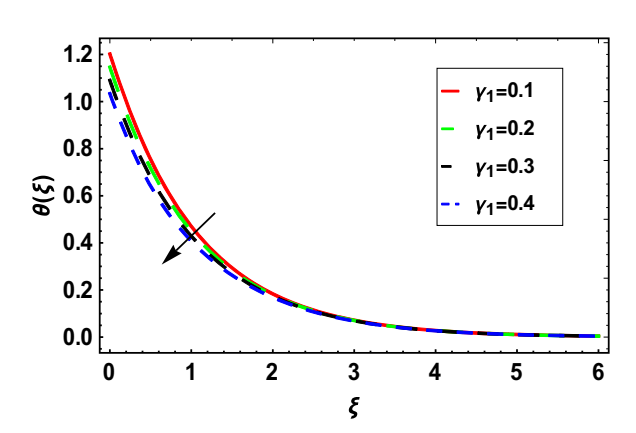


Figure 10: Variation in the temperature profile $\theta(\xi)$ *via* the thermal relaxation parameter y_1 .

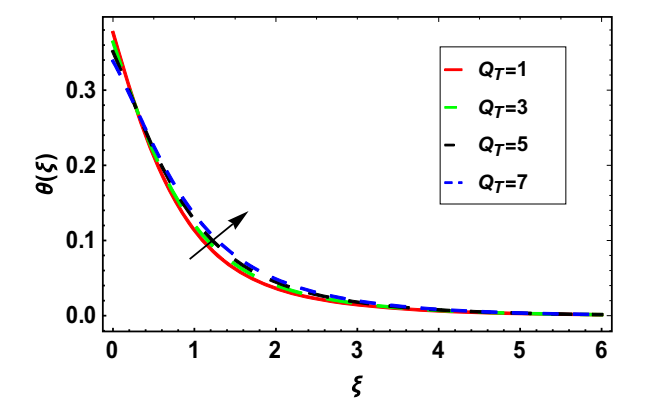


Figure 8: Variation in the temperature profile $\theta(\xi)$ *via* the thermal heat source parameter Q_T .

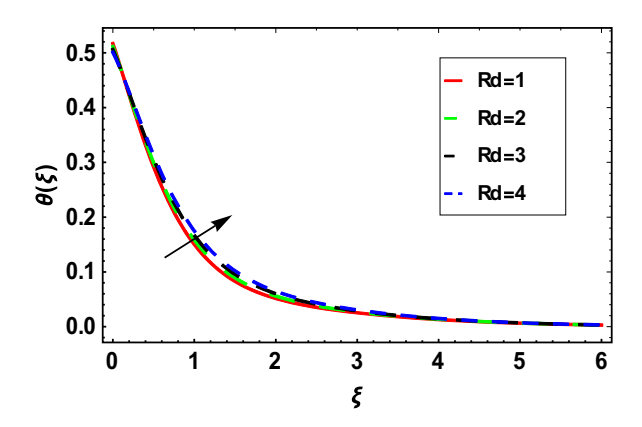


Figure 11: Variation in the temperature profile $\theta(\xi)$ *via* the thermal radiation parameter Rd.

slip factor, certain stretching velocities imparted to the liquid particles result in the retardation of fluid motion in all directions. The slip factors reduced the momentum boundary layers along both directions, which resulted in the decrease of $f'(\xi)$ and $g'(\xi)$. Figure 6 shows the behavior

of the modified Hartman number on the velocity profile. The velocity profile shows an increasing effect through a higher modified Hartman number. With a higher modified Hartman number, the momentum boundary layer thickness increases which in turn increases the velocity profile $f'(\xi)$.

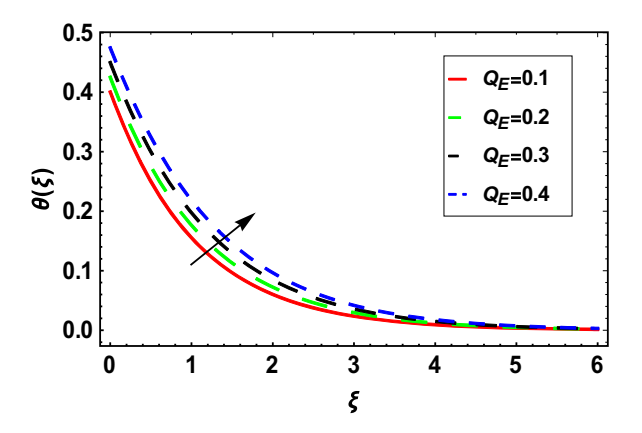


Figure 9: Variation in the temperature profile $\theta(\xi)$ *via* the exponential heat source parameter Q_E .

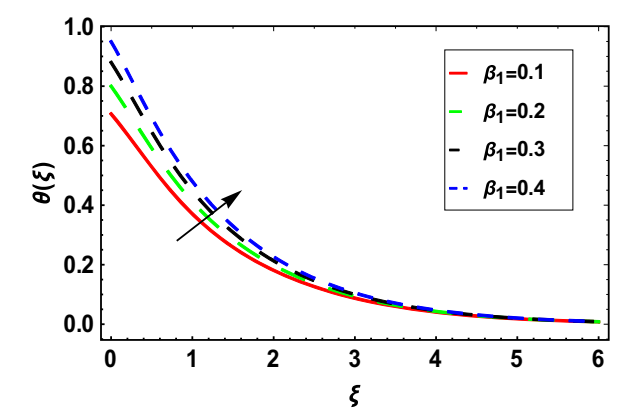


Figure 12: Variation in the temperature profile $\theta(\xi)$ *via* the thermal Biot number β_1 .

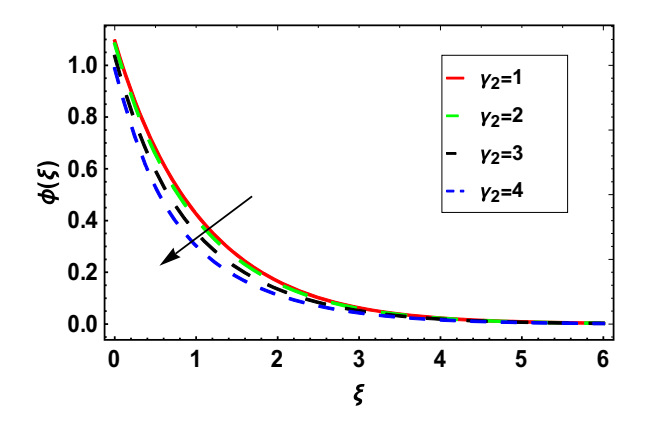


Figure 13: Variation in the concentration profile $\phi(\xi)$ *via* the mass relaxation parameter y_2 .

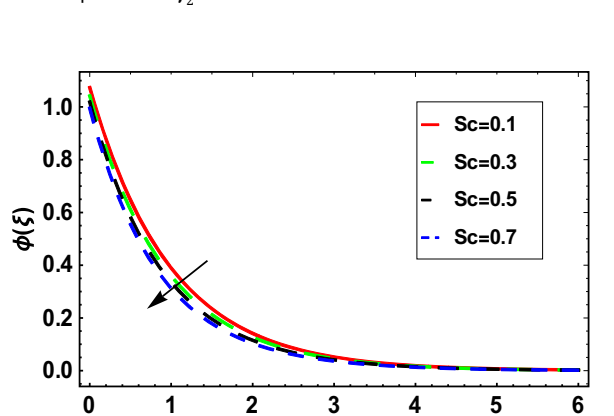


Figure 14: Variation in the concentration profile $\phi(\xi)$ *via* the Schmidt number Sc.

ξ

Figure 7 shows the effect of the ratio factor on $g'(\xi)$, which has an increasing influence on $g'(\xi)$. This is because there is a direct proportionality between the ratio factor λ and stretching velocity constant b. Due to this reason, an increasing trend is seen in $g'(\xi)$.

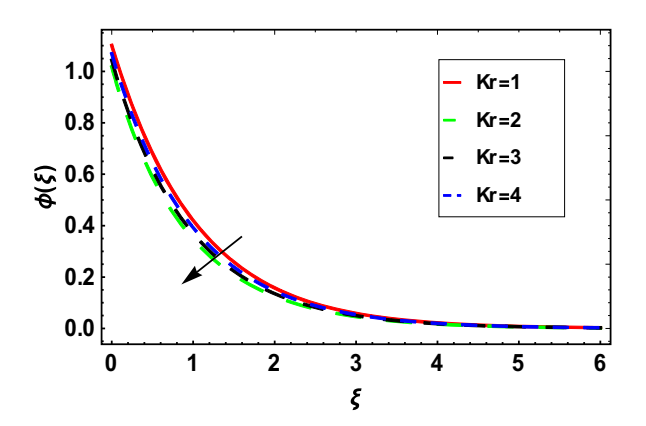


Figure 15: Variation in the concentration profile $\phi(\xi)$ *via* the chemical reaction parameter ${\rm Kr.}$

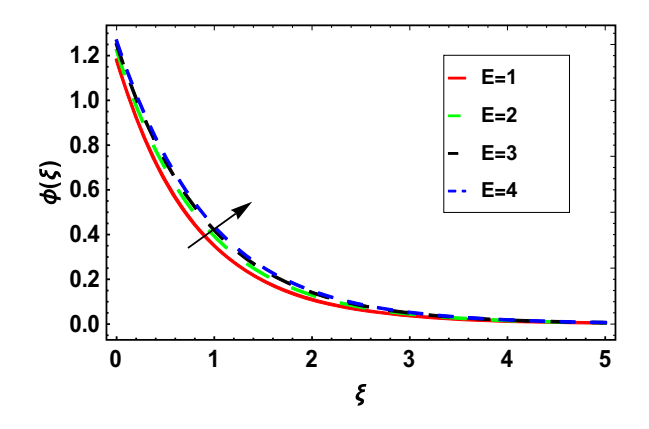


Figure 16: Variation in the concentration profile $\phi(\xi)$ *via* the activation energy parameter E.

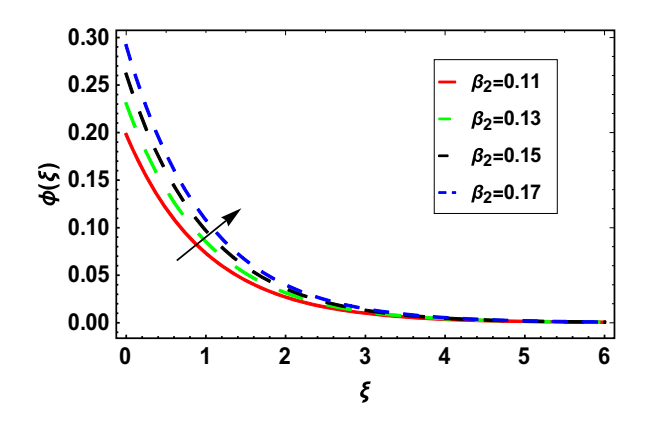


Figure 17: Variation in the concentration profile $\phi(\xi)$ *via* the concentration Biot number β_2 .

5.2 Temperature profiles

Figures 8 and 9 show the outcomes of the thermal and exponential heat source factors on the thermal profiles. Since the heat source parameter explains the heat

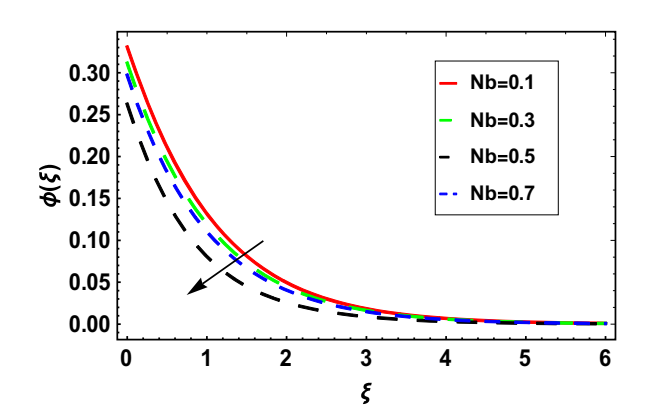


Figure 18: Variation in the concentration profile $\phi(\xi)$ *via* the Brownian motion parameter Nb.

10 — Humaira Yasmin et al. DE GRUYTER

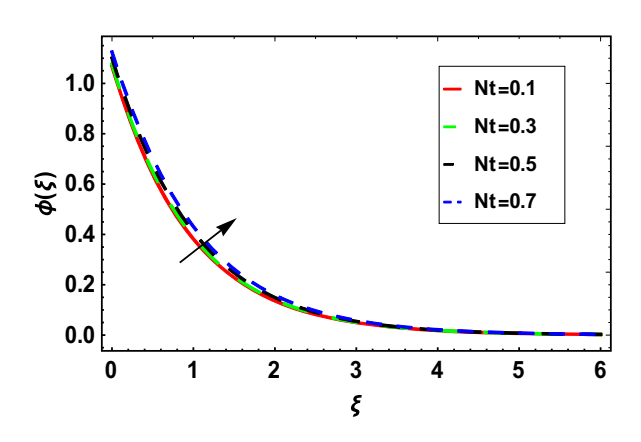


Figure 19: Variation in the concentration profile $\phi(\xi)$ *via* the thermophoresis parameter Nt.

production in the system, it is predicted that $\theta(\xi)$ will be increased with the growth of the heat source factors. Figure 10 shows the reducing influence of the thermal relaxation factor on the thermal profile. This is because the material particles require more time to pass heat to their adjacent sides. Also, the higher thermal relaxation factor shows a non-conducting behavior, which causes the decay in the thermal profile. The behavior of Rd on $\theta(\xi)$ is shown in Figure 11, which presents an increased behavior in the temperature distribution. The increase in Rd indicates the increase in the volume of heat radiated from the sheet and this heat is again absorbed by the hybrid nanofluid. Thus, the increasing behavior is observed in $\theta(\xi)$. Figure 12 shows the effect of the thermal Biot number on $\theta(\xi)$. An increasing tendency is observed in $\theta(\xi)$. The thermal resistance occurs among the nanoparticles at the surface of the Riga plate, which explains the intensification of the thermal scattering at the Riga surface, which increases the temperature profile $\theta(\xi)$.

Table 3: Comparison of the present results with previously published results for different values of λ when all other parameters are zero

λ	-f'	- <i>f</i> "(0)		<i>-g</i> "(0)	
	Bilal Ashraf et al. [44]	Present results	Bilal Ashraf et al. [44]	Present results	
0.0	1.000000	1.000000	0.000000	0.000000	
0.1	1.020260	1.020260	0.066847	0.066847	
0.2	1.039495	1.039495	0.148737	0.148737	
0.3	1.057955	1.057955	0.243360	0.243360	
0.4	1.075788	1.075788	0.349208	0.349208	
0.5	1.093095	1.093095	0.465205	0.465205	
0.6	1.109946	1.109946	0.590528	0.590528	
0.7	1.126397	1.126397	0.724532	0.724532	

Table 4: Numerical results of $\operatorname{Re}_{x}^{\frac{1}{2}}C_{fx}$ and $\operatorname{Re}_{y}^{\frac{1}{2}}C_{fy}$ for different values of Π_{1} and Π_{2} for the nanofluid and hybrid nanofluid

Π_1	II_2	$\Pi_1 = \Pi_2$	$\operatorname{Re}_{x}^{\frac{1}{2}}C_{fx}$	$\operatorname{Re}_{y}^{\frac{1}{2}}C_{fy}$
0.01			0.496072	0.533125
0.02			0.5111	0.550863
0.03			0.525928	0.567931
0.04			0.540556	0.584308
	0.01		0.528494	0.59307
	0.02		0.572849	0.670668
	0.03		0.614665	0.747638
	0.04		0.654523	0.823918
		0.01	0.54336	0.610765
		0.02	0.602194	0.704113
		0.03	0.658681	0.794561
		0.04	0.713755	0.881822

Table 5: Impact of λ , α_1 , and α_2 on $\operatorname{Re}_x^{\frac{1}{2}} C_{fx}$ and $\operatorname{Re}_y^{\frac{1}{2}} C_{fy}$

λ	a_1	a_2	$\operatorname{Re}_{x}^{\frac{1}{2}}C_{fx}$	$\operatorname{Re}_{y}^{\frac{1}{2}}C_{fy}$
0.2			0.54336	0.71162
0.3			0.56236	0.812475
0.4			0.57126	0.91333
	0.2		0.403535	_
	0.3		0.291494	_
	0.4		0.200147	_
		0.2	_	0.522499
		0.3	_	0.453119
		0.4	_	0.397523

5.3 Concentration profiles

The effect of γ_2 on $\phi(\xi)$ is shown in Figure 13. A declining tendency is seen here. The mass relaxation factor is used as

Table 6: Numerical results of $\operatorname{Re}_x^{\frac{-1}{2}}\operatorname{Nu}_x$ for different values of \varPi_1 and \varPi_2 for the nanofluid and hybrid nanofluid

II_1	II_2	$\Pi_1 = \Pi_2$	$Re_x^{\frac{-1}{2}}Nu_x$
0.01			0.19493
0.02			0.196474
0.03			0.197741
0.04			0.198725
	0.01		0.194937
	0.02		0.196492
	0.03		0.197774
	0.04		0.198778
		0.01	0.196483
		0.02	0.198752
		0.03	0.199873
		0.04	0.199984

Table 7: Impact of Rd, γ_1 , and β_1 on Re x^2 Nu_x

Rd	γ_1	$oldsymbol{eta_1}$	$Re_x^{\frac{-1}{2}}Nu_x$
0.6			0.170308
0.7			0.170911
0.8			0.171515
	0.2		0.187027
	0.3		0.177572
	0.4		0.168117
		0.2	0.388611
		0.3	0.569451
		0.4	0.737999

an indicator for the increase in time required for mass diffusion from the area of upper to lower concentration. The higher y_2 indicates that a large time is required for transferring mass from an upper region to a lower region, which consequently decreases the concentration of the hybrid nanofluid. Figure 14 shows the effect of the Schmidt number on $\phi(\xi)$. The Schmidt number and Brownian diffusion coefficient have an inverse relation with each other. Therefore, with higher Sc, the concentration profile and the concentration boundary layer thickness decrease. The increase in Kr decreases the chemical molecular diffusivity, and less diffusion occurs over the mass passage in the reactive flow, and the concentration profile decreases with the increase Sc. The increased values of Kr decreases $\phi(\xi)$ as shown in Figure 15. The increase in Kr causes the delay of mass diffusion, which decreases the concentration boundary layer thickness. Figure 16 shows the effect of the activation energy factor in decreasing the concentration profile. A majority of molecules that involve a minor amount of energy help diffusion of mass with the increase in E. Thus, the concentration profile increases with the increase in E values. Figure 17 shows the effect of the concentration Biot number on the mass profile. An increase in the concentration profile via the concentration Biot

Table 8: Impact of Sc, γ_2 , and β_2 on $\operatorname{Re}_x^{\frac{-1}{2}}\operatorname{Sh}_x$

Sc	\mathcal{V}_2	$oldsymbol{eta}_2$	$\operatorname{Re}_{x}^{\frac{-1}{2}}\operatorname{Sh}_{x}$
0.6			0.443151
0.7			0.443147
0.8			0.443144
	0.2		0.180788
	0.3		0.180754
	0.4		0.18072
		0.2	0.331942
		0.3	0.460122
		0.4	0.570216

number is shown. The larger Biot number increases the concentration distribution, which causes an increase in the concentration boundary layer thickness. Figure 18 shows how the mass concentration behaves for Nb. A decreasing influence of Nb on $\phi(\xi)$ is observed here. Physically with larger Nb, the random dispersion of nanoparticles increases in the liquid, causing the increase of kinetic energy of nanoparticles, which consequently decreases the mass concentration profile. The variation in $\phi(\xi)$ via Nt is shown in Figure 19. The concentration field increases with higher values of Nt. Physically, the higher Nt causes the nanoparticles concentration from a higher concentration region to a lower concentration region, which increases $\phi(\xi)$.

5.4 Discussion of tables

Table 3 shows the comparison of the present results with the previously published results for different values of λ when all other parameters are zero. From this table, we observe that the results of the present investigation are closely related to those of published results, which confirm the validity of the current investigation. Tables 4–8 signify the physical factors such as slip factor, volume fraction, thermal and concentration Biot number, Schmidt number, and thermal radiation parameters that affect the skin friction, heat transfer rate, and mass transfer rate. Table 4 lists

the results of the volume fraction on $Re_x^{\frac{1}{2}}C_{fx}$ and $Re_y^{\frac{1}{2}}C_{fy}$. With the increasing volume fraction, the nanoparticles collide with each other and lead to an increase in the fluid motion. Hence, the momentum boundary layer thickness decreases, and as a result the drag force at the surface increases. Table 5 shows the numerical result of skin friction through the slip and stretching ratio parameters. The increased slip causes a decrease in the skin friction and the increasing stretching rate increases the skin friction. It is known that the shear rate increases with an increase in the stretching rate, which results in higher skin friction. Table 6 shows the result of the effect of the volume fractions on

 $\mathrm{Re}_x^{\frac{-1}{2}}\mathrm{Nu}_x$. With increasing volume fractions, the thermal conductivities of the nanofluids and hybrid nanofluids increase, which has an increasing impact on the heat transfer rate. Table 7 displays the behavior of distinct para-

meters such as Rd, γ_1 , and β_1 on $\operatorname{Re}_x^{\frac{-1}{2}}\operatorname{Nu}_x$. An increase in Rd causes an increase in $\operatorname{Re}_x^{\frac{-1}{2}}\operatorname{Nu}_x$. It is because the resistive strength of the fluid motion increases with the higher

heat flux. The effects of Sc, γ_2 and β_2 on $\operatorname{Re}_x^{\frac{-1}{2}}\operatorname{Sh}_x$ is shown in Table 8, which indicates that higher values of Sc and γ_2

values of Rd. The thermal Biot number increased the

decrease $Re_x^{\frac{-1}{2}}Sh_x$ while higher values of β increase $Re_x^{\frac{-1}{2}}Sh_x$.

Conflict of interest: The authors state no conflict of interest.

Data availability statement: The data that support the findings of this study are available from the corresponding author upon reasonable request.

6 Conclusion

In the present analysis, we reflected the 3D EMHD flow of a copper–aluminum/water hybrid nanofluid flow on a Riga plate. The heat and mass flux model proposed by Cattaneo–Christov is deliberated here. The influences of thermal radiation, thermophoretic diffusion, Brownian motion, and chemical reactions are considered in the energy and concentration equation. The velocity slips, thermal convective, and mass convective conditions are adapted in this analysis. Suitable resemblance variables are implemented for the conversion of modeled equations to reduce the PDEs into ODEs. During the transformations of the set of nonlinear PDEs into ODEs, some physical parameters appeared, which are discussed physically. Some of the key points from the present analysis are the following:

- The results indicate that the slip factors have a decreasing impact on the velocity and skin friction coefficients, while the increasing modified Hartman number increases the velocity profile along the primary direction.
- An increasing behavior is observed in the thermal and heat transfer profiles through the maximum values of thermal radiation and thermal Biot number.
- 3) The concentration profile and mass transfer rate are increased with an increase in the solutal Biot number.
- 4) The concentration profile increases with the activation energy factor, while an opposite effect of the chemical reaction factor on the concentration profile is observed.
- 5) The skin friction increases with the estimated values of the stretching ratio factor.
- 6) The mass and thermal transfer rates are increased *via* higher values of thermal and solutal relaxation factors.

Funding information: The authors extend their appreciation to the Deanship of Scientific Research at King Khalid University, Abha, Saudi Arabia, for funding this work through the Research Group Project under Grant Number RGP.1/505/44. This work was supported by the Deanship of Scientific Research, the Vice Presidency for Graduate Studies and Scientific Research, King Faisal University, Saudi Arabia (Grant No. 5367).

Author contributions: All authors have accepted responsibility for the entire content of this manuscript and approved its submission.

References

- [1] Choi SUS, Eastman JA. Enhancing thermal conductivity of fluids with nanoparticles. 1995 Int Mech Eng Congr Exhib San Fr CA (United States); 12–17 Nov 1995. 1995 Oct 1 [accessed 2 Oct 2021]. https://digital.library.unt.edu/ark:/67531/metadc671104/.
- [2] Ayub M, Abbas T, Bhatti MM. Inspiration of slip effects on electromagnetohydrodynamics (EMHD) nanofluid flow through a horizontal Riga plate. Eur Phys J Plus. 2016;131(6):1–9.
- [3] Pal D, Mandal G. Magnetohydrodynamic stagnation-point flow of Sisko nanofluid over a stretching sheet with suction. Propuls Power Res. 2020;9(4):408–22.
- [4] Bhatti MM, Michaelides EE. Study of Arrhenius activation energy on the thermo-bioconvection nanofluid flow over a Riga plate. J Therm Anal Calorim. 2021;143(3):2029–38.
- [5] Ahmad S, Coban HH, Khan MN, Khan U, Shi Q-H, Muhammad T, et al. Computational analysis of the unsteady 3D chemically reacting MHD flow with the properties of temperature dependent transpose suspended Maxwell nanofluid. Case Stud Therm Eng. 2021;26:101169.
- [6] Hussain A, Arshad M, Rehman A, Hassan A, Elagan SK, Ahmad H, et al. Three-dimensional water-based magneto-hydrodynamic rotating nanofluid flow over a linear extending sheet and heat transport analysis: A numerical approach. Energies. 2021;14(16):5133.
- [7] Makinde OD, Aziz A. Boundary layer flow of a nanofluid past a stretching sheet with a convective boundary condition. Int J Therm Sci. 2011;50(7):1326–32.
- [8] Khan MR, Mao S, Deebani W, Elsiddieg AMA. Numerical analysis of heat transfer and friction drag relating to the effect of Joule heating, viscous dissipation and heat generation/absorption in aligned MHD slip flow of a nanofluid. Int Commun Heat Mass Transf. 2022;131:105843.
- [9] Devi SPA, Devi SSU. Numerical investigation of hydromagnetic hybrid Cu–Al2O3/water nanofluid flow over a permeable stretching sheet with suction. Int J Nonlinear Sci Numer Simul. 2016;17(5):249–57.
- [10] Yousefi M, Dinarvand S, Yazdi ME, Pop I. Stagnation-point flow of an aqueous titania-copper hybrid nanofluid toward a wavy cylinder. Int J Numer Methods Heat Fluid Flow. 2018;28(7):1716–35.
- [11] Swain K, Mebarek-Oudina F, Abo-Dahab SM. Influence of MWCNT/ Fe3O4 hybrid nanoparticles on an exponentially porous shrinking sheet with chemical reaction and slip boundary conditions. J Therm Anal Calorim. 2022;147(2):1561–70.
- [12] Joshi N, Upreti H, Pandey AK. MHD Darcy-Forchheimer Cu-Ag/H₂O-C₂H6O₂ hybrid nanofluid flow via a porous stretching sheet with suction/blowing and viscous dissipation. Int J Comput Methods Eng Sci Mech. 2020;23(6):527–35.
- [13] Ramzan M, Dawar A, Saeed A, Kumam P, Watthayu W, Kumam W. Heat transfer analysis of the mixed convective flow of

- magnetohydrodynamic hybrid nanofluid past a stretching sheet with velocity and thermal slip conditions. PLoS One. 2021;16(12):e0260854.
- [14] Dawar A, Islam S, Shah Z. A comparative analysis of the performance of magnetised copper–copper oxide/water and copper–copper oxide/kerosene oil hybrid nanofluids flowing through an extending surface with velocity slips and thermal convective conditions. Int | Ambient Energy. 2022;43(4):52.
- [15] Ghadikolaei SS, Hosseinzadeh K, Hatami M, Ganji DD. MHD boundary layer analysis for micropolar dusty fluid containing Hybrid nanoparticles (Cu-Al2O3) over a porous medium. J Mol Liq. 2018;268:813–23.
- [16] Gul T, Qadeer A, Alghamdi W, Saeed A, Mukhtar S, Jawad M. Irreversibility analysis of the couple stress hybrid nanofluid flow under the effect of electromagnetic field. Int J Numer Methods Heat Fluid Flow. 2021;32(2):642–59.
- [17] Md Basir MF, Mackolil J, Mahanthesh B, Nisar KS, Muhammad T, Anuar NS, et al. Stability and statistical analysis on melting heat transfer in a hybrid nanofluid with thermal radiation effect. Proc Inst Mech Eng Part E J Process Mech Eng. 2021;235(6):2129–40.
- [18] Rasool G, Shafiq A, Khalique CM. Marangoni forced convective Casson type nanofluid flow in the presence of Lorentz force generated by Riga plate. Discret Contin Dyn Syst. 2021;14(7):2517.
- [19] Naseem A, Shafiq A, Zhao L, Farooq MU. Analytical investigation of third grade nanofluidic flow over a riga plate using Cattaneo-Christov model. Results Phys. 2018;9:961–9.
- [20] Khashi'ie NS, Arifin NM, Pop I, Wahid NS. Effect of suction on the stagnation point flow of hybrid nanofluid toward a permeable and vertical Riga plate. Heat Transf. 2021;50(2):1895–910.
- [21] Alotaibi H, Rafique K. Numerical Analysis of Micro-Rotation Effect on Nanofluid Flow for Vertical Riga Plate. Crystals. 2021;11(11):1315.
- [22] Ahmed N, Saba F, Khan U, Khan I, Alkanhal TA, Faisal I, et al. Spherical shaped ($Ag-Fe_3O_4/H_2O$) hybrid nanofluid flow squeezed between two Riga plates with nonlinear thermal radiation and chemical reaction effects. Energies. 2018;12(1):76.
- [23] Rehman KU, Shatanawi W, Al-Mdallal QM. A comparative remark on heat transfer in thermally stratified MHD Jeffrey fluid flow with thermal radiations subject to cylindrical/plane surfaces. Case Stud Therm Eng. 2022;32:101913.
- [24] Eid MR, Nafe MA. Thermal conductivity variation and heat generation effects on magneto-hybrid nanofluid flow in a porous medium with slip condition. Waves Random Complex Media. 2022;32(3):1103–27.
- [25] Ashraf W, Khan I, Andualem M. Thermal transport investigation and shear drag at solid–liquid interface of modified permeable radiative-SRID subject to Darcy–Forchheimer fluid flow composed by y-nanomaterial. Sci Rep. 2022;12(1):1–12.
- [26] Mandal G. Convective-radiative heat transfer of micropolar nanofluid over a vertical non-linear stretching sheet. J Nanofluids. 2016;5(6):852–60.
- [27] Saeed A, Algehyne EA, Aldhabani MS, Dawar A, Kumam P, Kumam W. Mixed convective flow of a magnetohydrodynamic Casson fluid through a permeable stretching sheet with first-order chemical reaction. PLoS One. 2022;17(4):e0265238.
- [28] Dawar A, Islam S, Shah Z, Mahmuod SR, Lone SA. Dynamics of interparticle spacing, nanoparticle radius, inclined magnetic field and nonlinear thermal radiation on the water-based copper nanofluid flow past a convectively heated stretching surface with mass flux condition: A strong suction case. Int Commun Heat Mass Transf. 2022;137:106286.

- [29] Shah NA, Tosin O, Shah R, Salah B, Chung JD. Brownian motion and thermophoretic diffusion effects on the dynamics of MHD upper convected Maxwell nanofluid flow past a vertical surface. Phys Scr. 2021;96(12):125722.
- [30] Kalpana G, Madhura KR, Kudenatti RB. Magnetohydrodynamic boundary layer flow of hybrid nanofluid with the thermophoresis and Brownian motion in an irregular channel: A numerical approach. Eng Sci Technol Int J. 2021;101075.
- [31] Iqbal Z, Khan M, Ahmed A, Nadeem S. Features of thermophoretic and Brownian forces in Burgers fluid flow subject to Joule heating and convective conditions. Phys Scr. 2020;96(1):15211.
- [32] Shah NA, Wakif A, El-Zahar ER, Ahmad S, Yook S-J. Numerical simulation of a thermally enhanced EMHD flow of a heterogeneous micropolar mixture comprising (60%)-ethylene glycol (EG),(40%)water (W), and copper oxide nanomaterials (CuO). Case Stud Therm Eng. 2022;102046.
- [33] Ali B, Nie Y, Hussain S, Manan A, Sadiq MT. Unsteady magneto-hydrodynamic transport of rotating Maxwell nanofluid flow on a stretching sheet with Cattaneo-Christov double diffusion and activation energy. Therm Sci Eng Prog. 2020 Dec;20:100720. doi: 10. 1016/J.TSEP.2020.100720.
- [34] Umar M, Akhtar R, Sabir Z, Wahab HA, Zhiyu Z, Imran A, et al. Numerical treatment for the three-dimensional Eyring-Powell fluid flow over a stretching sheet with velocity slip and activation energy. Adv Math Phys. 2019;2019.
- [35] Takabi B, Salehi S. Augmentation of the heat transfer performance of a sinusoidal corrugated enclosure by employing hybrid nanofluid. Adv Mech Eng. 2014;2014. doi: 10.1155/2014/147059.
- [36] Hayat T, Nadeem S, Khan AU. Rotating flow of Ag-CuO/H2O hybrid nanofluid with radiation and partial slip boundary effects. Eur Phys J E. 2018 Jun;41(6):1–9. https://link.springer.com/article/doi: 10. 1140/epje/i2018-11682-y.
- [37] Oztop HF, Abu-Nada E. Numerical study of natural convection in partially heated rectangular enclosures filled with nanofluids. Int J Heat Fluid Flow. 2008 Oct;29(5):1326–36. doi: 10.1016/J. IJHEATFLUIDFLOW.2008.04.009.
- [38] Sheikholeslami M, Gorji-Bandpy M, Ganji DD. Numerical investigation of MHD effects on Al2O3–water nanofluid flow and heat transfer in a semi-annulus enclosure using LBM. Energy. 2013 Oct;60:501–10. doi: 10.1016/J.ENERGY.2013.07.070.
- [39] Hayat T, Ahmed B, Abbasi FM, Alsaedi A. Hydromagnetic peristalsis of water based nanofluids with temperature dependent viscosity: a comparative study. J Mol Liq. 2017;234:324–9.
- [40] Liao SJ. On the proposed homotopy analysis technique for nonlinear problems and its applications. Shanghai Jiao Tong University; 1992.
- [41] Liao S-J. A uniformly valid analytic solution of two-dimensional viscous flow over a semi-infinite flat plate. J Fluid Mech. 1999;385:101–28.
- [42] Liao S-J. On the analytic solution of magnetohydrodynamic flows of non-Newtonian fluids over a stretching sheet. J Fluid Mech. 2003;488:189–212.
- [43] Saeed Khan N, Gul T, Islam S, Khan A, Shah Z. Brownian motion and thermophoresis effects on MHD mixed convective thin film secondgrade nanofluid flow with Hall effect and heat transfer past a stretching sheet. J Nanofluids. 2017;6:812–29. https://www. ingentaconnect.com/contentone/asp/jon/2017/00000006/ 00000005/art00003.
- [44] Bilal Ashraf M, Hayat T, Alhuthali MS. Three-dimensional flow of maxwell fluid with soret and dufour effects. J Aerosp Eng. 2016;29(3):4015065.